

Phase and grain size engineering in Ge-Sb-Te-O by alloying with La-Sr-Mn-O towards improved material properties

Nikolas Kraft^{a,b}, Guoxiang Wang^{c,d,*}, Hagen Bryja^a, Andrea Prager^a, Jan Griebel^a, Andriy Lotnyk^{a,c,*}

^a Leibniz Institute of Surface Engineering (IOM), Permoserstr. 15, D-04318 Leipzig, Germany

^b Leipzig University, Faculty for Chemistry and Mineralogy, Johannisalle 29, 04103 Leipzig, Germany

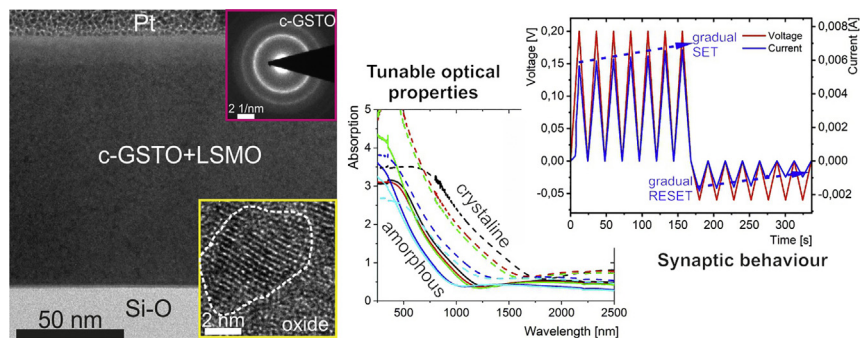
^c Laboratory of Infrared Materials and Devices, The Research Institute of Advanced Technologies, Ningbo University, Ningbo, Zhejiang 315211, China

^d Zhejiang Key Laboratory of Photoelectric Detection Materials and Devices, Ningbo University, Ningbo, Zhejiang 315211, China

HIGHLIGHTS

- Preparation of Ge-Sb-Te-O thin films alloyed with La-Sr-Mn-O oxide
- Suppression of grain growth and in the formation of stable phase
- Alloying enhances thermal stability and resistivity of the thin films
- Composites reveal synaptic behavior and tunable optical properties

GRAPHICAL ABSTRACT



ARTICLE INFO

Article history:

Received 9 September 2020

Received in revised form 6 November 2020

Accepted 6 December 2020

Available online 8 December 2020

Keywords:

Phase change alloy

Memory materials

Neuro-inspired computing

Bipolar resistive switching

Transmission electron microscopy

ABSTRACT

Ge-Sb-Te alloys are promising materials for non-volatile memory applications. Alloying of the materials with various elements is considered as prospective approach to enhance material properties. This work reports on the preparation and characterization of pure Ge-Sb-Te-O (GSTO) and alloyed with La-Sr-Mn-O (LSMO) thin films. Thermal heating of amorphous thin films to different temperatures show distinct crystallization behavior. A general trend is the decrease in the size of GSTO crystallites and the suppression in the formation of stable trigonal GSTO phase with increasing content of LSMO. Microstructural studies by transmission electron microscopy show the formation of metastable GSTO nanocrystallites dispersed in the amorphous matrix. Analysis of local chemical bonding by X-ray spectroscopy reveal the presence of different oxides in the GSTO-LSMO composites. Moreover, the composites with a high LSMO content exhibit higher crystallization temperature and significant larger sheet resistance in amorphous and crystalline phase, while a memory device made of GSTO-LSMO alloy reveals bipolar switching and synaptic behavior. In addition, the amount of LSMO in GSTO-LSMO thin films influences their optical properties and band gap. Overall, the results of this work reveal the highly promising potential of GSTO-LSMO nanocomposites for data storage and reconfigurable photonic applications as well as neuro-inspired computing.

© 2020 The Author(s). Published by Elsevier Ltd. This is an open access article under the CC BY license (<http://creativecommons.org/licenses/by/4.0/>).

* Corresponding authors.

E-mail addresses: wanguoxiang@nbu.edu.cn (G. Wang), andriy.lotnyk@iom-leipzig.de (A. Lotnyk).

1. Introduction

Non-volatile memory is one of the key components that support the electronic information industry such as network communication, high performance computing and digital applications as well as consumer electronics development. Ge-Sb-Te (GST)-based phase change materials (PCMs) are promising alloys for optical and electronic memory applications [1–5]. The PCMs have excellent properties including non-volatility, scalability, large property contrast, fast operation times and compatibility with existing CMOS technology [6].

Memory devices based on GST thin layers use the reversible phase transitions between the crystalline and amorphous phases in these alloys. The transitions are typically induced either by Joule or laser-beam heating and are associated with changing in physical properties of the alloys (e.g. resistance, optical reflectivity). For memory applications, PCM based memory devices utilizes a large contrast either in electrical resistance or in optical reflectivity between the amorphous state and crystalline state. However, GST alloys suffer from several drawbacks, including insufficient data retention at high temperatures and high programming power of memory devices. These issues hinder the applications of GST materials in embedded memory devices, particularly in automotive and aerospace products. To meet the first requirement, the amorphous phase of GST materials must have a high crystallization temperature and activation energy, thus a high thermal stability of the GST alloys against spontaneous crystallization. However, low crystallization temperature of pure GST materials (between 140 and 160 °C) impacts the stability of the amorphous phase [7–9]. This makes GST alloys not suitable for the embedded applications [10]. Alloying of GST materials with widely used chemical elements like oxygen, carbon, nitrogen is a promising approach to enhance material properties and thus, to improve device characteristics, such as cycling endurance, higher temperature retention, writing speed and power consumption [10–13]. Particularly, the crystallization activation energy of the alloyed GST materials increases, which enhances crystallization temperature and thus, improves thermal stability of the amorphous phase [14–17]. In addition, the alloying suppresses grain growth, which enhances device endurance [13]. However, incorporation of additional elements into GST structure might lead to the decomposition of GST alloys, resulting in unwanted phase separation. For example, doping of GeSb₂Te₄ alloy with 10–15 at.% oxygen and Ge₂Sb₂Te₅ (GST225) thin films with 21.7%–30.8% oxygen resulted in the precipitation of Sb₂Te₃ secondary phase [15,18] as well as in the formation of GeO_x and SbO_x oxides in addition [19]. Though, the formation of additional oxides can be viewed as superior since the oxides provide additional nucleation sites for GST materials, which are nucleation-dominated materials [20,21]. Although doping with single elements is a promising approach to enhance the properties of electrical memory devices, co-doping with oxygen and nitrogen can improve the recording characteristics of optical disk used for optical memory applications [14,22].

With regard to the second requirement, the power consumption of GST based memory device depends on many factors. These are the cell design, the melting temperature, the switching volume, the electrical resistivity and the thermal conductivity of GST alloy. Particularly, the confinement of GST alloys or electrode materials largely led to the reductions in RESET current of PCM memory cells [4,6,23–26]. In addition, nano sized GST225 thin films (crystallites in the range between 10 and 17 nm) were used to enable memory devices with very fast switching times [27,28]. The thin films showed higher crystallization temperature, suggesting faster interfacial growth rates and thus, faster switching times [27]. This is because interface-assisted crystallization of GST thin films is advantages over heterogenous nucleation [29]. However, thermal conductivity of GST phases is a fundamental property. It can be improved by appropriate material design. So, co-sputter deposition of GST225 and with oxides such as SiO₂, TiO_x, or TaO_x has shown to enhance not only the thermal stability of amorphous phase, but also to reduce the thermal conductivity of the composite, thus reduces heat

dissipation and reset current [30–32]. This effect can be attributed to the increase in the thermal boundary resistance (TBR) at the interface between GST and surrounding materials (e.g. dielectric oxide) [33]. Reifenberg et al. suggested that the combination of low thermal conductivity PCMs with high thermal conductivity materials might increase the TBR [33]. Moreover, GST225-oxide (mainly SiO₂, TiO_x, HfO_x, ZnO, PbZr_{0.30}Ti_{0.70}O₃) composite thin films revealed the formation of GST225 nanocrystals embedded into oxide matrix, resulting in an increased density of interfaces and nucleation sites as well as reduced size of working unit [21,30–32,34–37]. Interestingly, the alloying of GST225 with individual elements or oxides did not significantly influence the initial resistance of amorphous phase compared to the undoped GST. Only GST225-ZnO and GST225-HfO_x nanocomposites revealed two orders and one order of magnitude difference for highest oxide content compared to undoped samples, respectively. High resistive GST is essential to reduce the writing current of phase change memory devices [4,13].

This work reports on the preparation and study of the microstructure, local structure, electrical and optical properties of pure Ge-Sb-Te-O (GSTO) and alloyed with La-Sr-Mn-O (LSMO) thin films. The oxide is selected due its larger thermal conductivity (ranging between 2.8 and 4 W/mK) [38] as of pure GST alloys (0.2 W/mK for amorphous GST and 0.6 W/mK for cubic GST) [39,40]. In addition, the LSMO oxide shows interesting properties such as half-metallic properties and colossal magnetoresistance and thus, its suitable for spintronic applications [41–43]. Consequently, such GSTO-LSMO composites might show unexpected properties, which are out of scope of the present study and will be performed in the future. The outcomes of this work reveal that LSMO content influences crystallization behavior, thermal stability, electrical and optical properties of the GSTO-LSMO thin films.

2. Experimental

150-nm-thick pure GST and alloyed with the La-Sr-Mn-O oxide thin films were deposited on quartz and SiO₂/Si (100) substrates by magnetron co-sputtering using individual Ge₂Sb₂Te₅ (GST225) and La_{0.66}Sr_{0.33}MnO₃ (LSMO) targets at room temperature. First, the chamber was gradually evacuated to 2.3×10^{-4} Pa, then argon gas with a constant flow rate of 50 sccm was introduced into the chamber to achieve a working pressure of 0.25 Pa to deposit the thin films. During deposition, the O₂ reactant flow rate of 0.5 sccm was used for sputtering, resulting in the GSTO thin films. A radio frequency power (P_{rf}) of 60 W was applied to the GST225 target, whereas the direct current power (P_{dc}) applied to the LSMO target was 0 W, 8 W, 14 W and 21 W to tune the amount of LSMO in the GST225 thin films. The substrates were rotated in order to improve the thickness homogeneity of the films. The thickness of thin films was controlled using a thickness monitor equipped in the chamber and further confirmed by Veeco Dektak 150 surface profile-meter.

The sheet resistances of as-prepared thin films as a function of temperature were examined in situ at a heating rate of 40 °C/min by a four-probe method in a homemade vacuum chamber. The crystallization of amorphous samples was performed at various temperatures between 200 °C and 350 °C. The heating rates of 150 K/s and holding time of 10 min were used. For resistive switching device, Ag thin film was used as the bottom electrode while W tip with diameter of 15 μm was applied as the top electrode. The device was characterized with a Keithley 2600 source meter in DC current–voltage (I–V) sweep mode. The electric bias was applied to the bottom electrode, while the top electrode was grounded.

The preparation of cross-sectional specimens for TEM studies was performed by a combination of focused gallium (30 keV, 15 keV, 5 keV and 2 keV) and focused argon (900 eV and 500 eV at the LN₂ temperature) ion beam milling. The microstructure of LSMO-GST samples was studied in a probe Cs-corrected Titan³ G2 60–300 microscope operating at 300 kV accelerating voltage and equipped with X-FEG high brightness

electron source. Bright-field TEM images and selected area electron diffraction (SAED) patterns were acquired by using a Gatan US1000XP P CCD camera. Energy dispersive X-ray (EDX) analysis was done in scanning TEM (STEM) mode. A probe forming annular aperture of 20 mrad was used for STEM work. STEM images were recorded with a high-angle annular dark-field (HAADF) STEM detector using annular ranges of 80–200 mrad. The detector ranges fulfil the conditions corresponding to Z contrast imaging, in which atomic columns with a higher average Z number (e.g. Te ($Z = 52$) or Sb ($Z = 51$)) in HAADF images appear brighter than those elements with a lower average Z number (e.g. Ge ($Z = 32$)). EDX maps were recorded with a FEI Super-X EDX detector system using Bruker processing software. The accuracy in determination of element concentration is ± 0.1 at.%. The beam currents were set to 150 pA during the EDX mapping.

X-ray photoelectron spectroscopy (XPS) analyses were carried out on an Axis Ultra (Kratos Analytical, Ltd., Manchester, UK) with a monochromatic Al excitation source at 150 W (15 kV, 10 mA). Survey spectra were collected at 160 eV pass energy with 1.0 eV nominal resolution. High resolution spectra were measured by 40 eV pass energy with 0.1 eV nominal resolution. The studied thin films were bombarded with Ar-ions for at least 3 min. In this way, the atoms near the surface were removed to obtain a clean and un-oxidized surface of the studied samples.

The UV/VIS/NIR spectra were recorded with a spectral photometer CARY 5000 (AGILENT) in the range 250–2500 nm with a scan rate of 600 nm/min. A piece of SiO₂ glass with same thickness as the substrate was used as the reference material to calculate the absorption in thin films.

3. Results and discussion

3.1. Chemical composition

The characterization of the studied samples is started with the description of their chemical compositions. EDX mapping was used to quantify the concentration of elements in the studied composite samples. The distribution of elements in as-deposited and crystallized thin films over the thickness is shown in the Supporting Information (see Fig. S1 and S2). The area used for quantification of the samples was chosen carefully to obtain the information about the samples only, without considering any oxide layer, substrate and platinum layer (see Fig. S1 and S2). On top of every film was an oxide layer containing besides oxygen, mainly germanium and antimony. The composition of the studied samples is shown in Fig. 1. Every value is the average of three individual quantifications of EDX maps that were performed over 10 min to get a good signal to noise ratio. The samples deviate from the expected stoichiometry

Table 1
Optical parameters E_g^{opt} of amorphous and crystalline GSTO and GSTO-LSMO composite thin films.

Sample	E_g^{opt} , eV (RT)	E_g^{opt} , eV (200 °C)	E_g^{opt} , eV (350 °C)
GSTO	0.68	0.43	0.37
GSTO-LSMO (4 W)	0.69	0.43	0.40
GSTO-LSMO (8 W)	0.75	0.46	0.41
GSTO-LSMO (14 W)	0.77	0.47	0.41
GSTO-LSMO (21 W)	0.77	0.48	0.42

of the original GST225 target and contain more antimony than germanium. The average Ge/Sb/Te ratio was measured to be $2/2.4/4.6 \pm 0.3$ (Fig. 1a). (See Table 1.)

The La/Sr/Mn/O ratio also does not represent the stoichiometry of the original La_{0.66}Sr_{0.33}MnO₃ target. The concentrations for lanthanum, strontium, manganese and oxygen increase with increasing co-sputtering power as expected (Fig. 1b and c). However average concentration of La, Sr and Mn is much lower comparing to average concentration of oxygen. Depending on the applied sputtering power to the LSMO target, the concentration of Sr varies between 0.1 and 0.3 at.% for sputtering powers of 4 W and 8 W, respectively, while the concentration of Sr is 0.7 and 0.9 at.% for sputtering powers of 14 and 21 W, respectively. The concentration of La is at 0.5 and 0.8–0.9 at.% for sputtering powers of 4 W and 8 W, respectively, whereas it is 1.6–1.7 and 1.7–2.1 at.% for sputtering powers of 14 and 21 W, respectively. The concentration of Mn is 0.2–0.4 and 0.3–0.7 at.% for sputtering powers 4 W and 8 W, respectively, whereas it is 0.7–1.8 and 1.6–2.2 at.% for sputtering powers of 14 and 21 W, respectively. Thus, the distribution of Mn concentration is broader compared to Sr and La. In addition, the concentration of three elements is rather low in the samples. Contrary, the oxygen concentration is rather high in all samples and cannot be explained by the oxygen originated from the LSMO target. The pure GST225 samples show oxygen contents of approximately 10 at.% and the notation GSTO will be used further in text. The oxygen content rise up to 29 at.% for sputtering power of 21 W for LSMO target. Consequently, the increase in oxygen content with increasing co-sputtering power is also higher than the stoichiometry of the target would explain. Since the target has the initial composition of La_{0.66}Sr_{0.33}MnO₃, the oxygen concentration should rise three times as much as the manganese concentration. The increase is in average 14 times the manganese increase, so it rises nearly four times faster than expected. This is due to the fabrication method of such samples. Since magnetron sputtering is non ultra-high vacuum method, the additional oxygen might derive from the atmosphere in the chamber. An increase of the oxygen content over time can be ruled out, because the comparison of oxygen concentration to one-year old

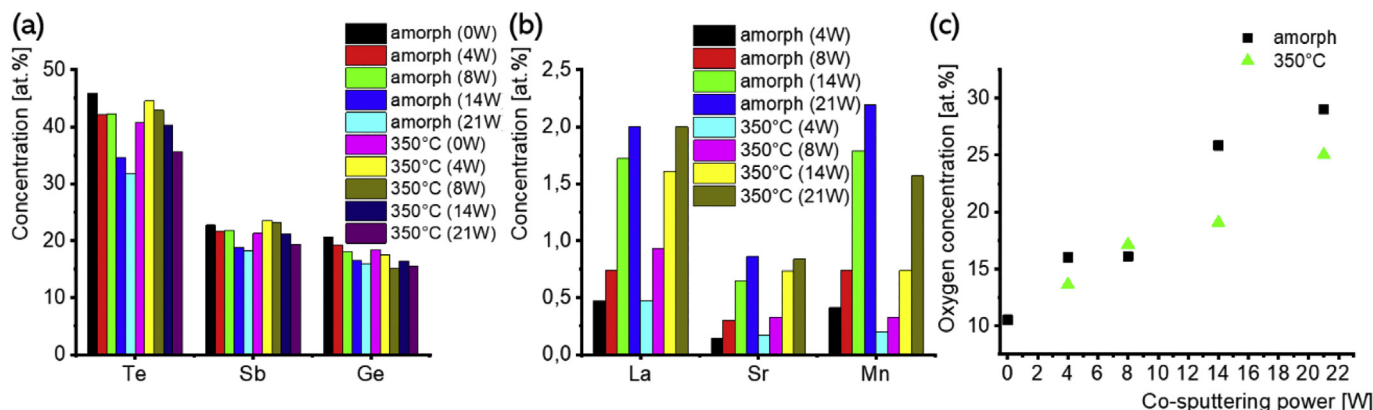


Fig. 1. Concentration of different elements in studied GSTO-LSMO composite thin films: (a) Te, Sb, Ge, (b) La, Sr, Mn and (c) O.

measurements showed no significant differences. Overall, it is expected that the influence of oxygen on the microstructure and properties of composite samples should be much pronounced than of the Sr, La and Mn elements. In addition, deposition systems with low oxygen background pressure can be used for preparation of Ge-Sb-Te samples with huge concentration of oxygen (up to 10 at.%).

3.2. Microstructural studies

The as-deposited GSTO and GSTO-LSMO composite samples across all co-sputtering powers are in amorphous state. Fig. 2(a) shows bright-field TEM image and SAED pattern of pure GSTO sample. The pattern shows diffuse rings, which are typical for amorphous materials. However, on a smaller scale, the local environment can still be ordered. All SAED images show two diffuse maxima at 3.3 nm^{-1} and 5.2 nm^{-1} which match to reported values for amorphous GST225. These are also roughly the regions in which the crystalline phases show their strong diffraction spots. Pure and composite samples crystallized at 200°C (GSTO200) are on a large scale crystalline. This can be concluded from the SEAD pattern, which show sharp diffraction spots instead of diffuse rings (Fig. 2(b)). Since every SAED reveals the diffraction spots of cubic phase, it can be supposed that all crystals are of metastable cubic phase. A preferred orientation cannot be seen in the diffractograms. Pure GSTO sample shows crystallites with sizes of up to 20 nm. The grains in the intermediately alloyed GSTO-LSMO(8 W) thin films are smaller (approximately 10 nm) and the GSTO-LSMO(21 W) sample shows the smallest crystallites (approximately 5 nm). GSTO exhibits no preferential nucleation sites. The difference in crystal grain size can also be seen in the SAEDs. Because of the statistical distribution of the crystals, the diffraction spots are ordered into rings around the primary beam. SAED patterns of highly alloyed composite samples (Fig. 2c) show continuous rings, while the pure sample (Fig. 2b) displays isolated diffraction spots, showing larger crystallites. Moreover, composite samples with smaller crystallites contain amorphous regions (Fig. 2(c)). These regions are oxides. HAADF-STEM images revealed dark spots, which are more distinct in the highly alloyed sample (Fig. 2(d)). If the specimen is assumed to be equally thick, the difference in brightness is caused by the Z^2 dependency of the scattered electrons. This means that bright areas contain heavy elements and the darker part consist of lighter elements such as oxygen. In addition, EDX lines scans (not shown) over such dark areas of composite samples showed that the areas are enriched in oxygen, manganese and lanthanum. A phase separation process is a possible explanation, where one phase contains heavier elements than the other. The detailed local environment of each element measured by XPS will be described below. Compared to crystal sizes (ranging between 30 and 60 nm) formed either in ex situ or laser crystallized oxygen-free GST225 thin films [44,45], nanocrystalline GSTO

thin films and GSTO-LSMO nanocomposites would be advantageous for phase-change applications. High density of nucleation sites provided by the oxide could enhance the nucleation rate of GSTO component, as has been reported for GST225-ZnO-nanocomposites [21]. In addition, due to the suppression of grain growth the cell endurance can also be enhanced as has been shown for N doped GST alloy [13].

GSTO samples crystallized at a temperature of 350°C differ from each other, depending on LSMO content. Like in the GSTO samples crystallized at a temperature of 200°C , the crystal size depends on sputtering power of LSMO target. With higher sputtering power, the crystals are smaller. The specimen with less LSMO lost contact to the substrate, producing hollow spaces at some areas. In addition, higher LSMO content influence phase formation of GST alloy. Pure GSTO sample crystallized at a temperature of 350°C contains crystallites ranging between 20 nm and 200 nm. In some parts large crystals grew into each other and filled the whole space (Fig. 3a). SAED pattern shows the diffraction spots of trigonal GST225 phase (Fig. 3b). Hollow spaces such as round voids are also formed between the thin film and the Si-O substrate. At such areas the thin film lost contact to the substrate. Similar voids were also reported in oxygen free GST225 samples crystallized at a temperature of 320°C [46]. However, their shape was pyramid-like and differs from the observed in this work. The formation of large voids observed in GSTO sample might be occurred during phase transition where an anisotropic elongation of trigonal large crystals occurs and is caused by strain release as well as volume shrinking during the phase transition. It should be noted that trigonal crystals close to these hollow spaces look plastically deformed and are formed with (0001) planes near parallel to the Si-Ox substrate, although some grains were inclined with (0001) plane with respect to the substrate surface. The microstructure of GSTO-LSMO(4 W) sample crystallized at a temperature of 350°C looks similar to the pure GSTO thin film. It also shows the formation of large voids with plastically deformed crystals at its rims. Contrary, GSTO-LSMO(8 W) thin film crystallized at the same temperature displays very small round voids where the thin film lost contact to the substrate. In this specimen there is coexisting of large trigonal and small cubic crystallites (Fig. 3c). However, diffraction spots of the trigonal phase belong to $\text{Ge}_1\text{Sb}_2\text{Te}_4$ with some remaining GST225 building units as was confirmed by atomic-resolution HAADF-STEM imaging (Fig. 3c). This is not surprising because chemically disorder in trigonal GST225 phase is typical for the phase and is in line with EDX quantifications. Some interesting feature in composition of cubic and trigonal crystallites was identified from EDX maps. The trigonal crystals are depleted in oxygen (12.6 at.%), while the cubic grains contain more oxygen (17.4 at.%). The areas with cubic phase display image contrast similar to the of Fig. 2d. Thus, it is reasonable to assume that dark areas in the figure are rich in oxygen. It worth to note that the concentration of oxygen in trigonal grains is very close to as-deposited

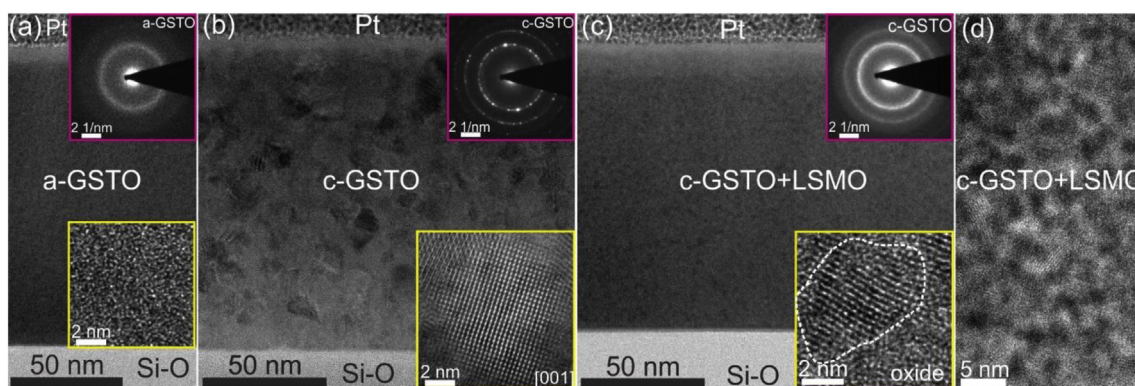


Fig. 2. (a) Bright-field TEM images of (a) as-deposited GSTO thin film and (b) crystallized at a temperature of 200°C . (c)-(d) Bright-field TEM and HAADF-STEM micrographs of GSTO-LSMO (21 W) composite thin film crystallized at a temperature of 200°C . Upper insets in (a)-(c) represent SAED patterns while lower insets are high-resolution images.

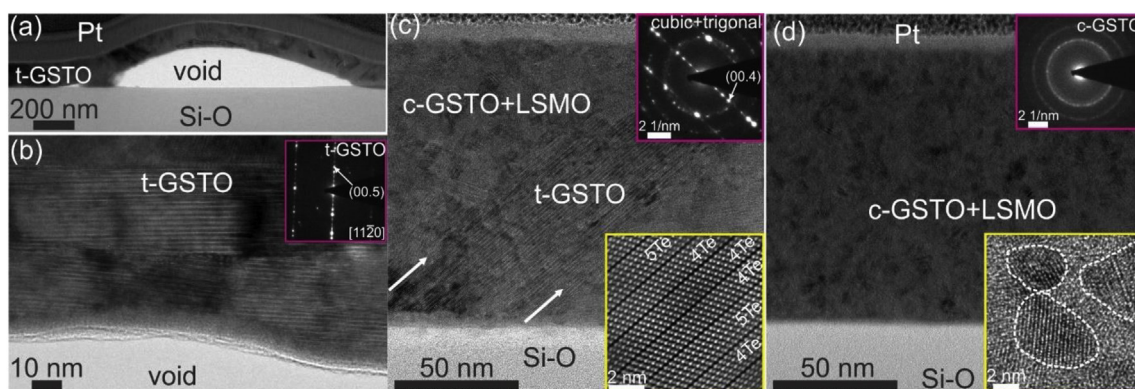


Fig. 3. (a)–(b) Bright-field TEM images of GSTO thin film crystallized at a temperature of 350 °C. (c) and (d) Bright-field TEM micrographs of GSTO-LSMO (8 W) and GSTO-LSMO (21 W) composite thin films crystallized at a temperature of 350 °C. Upper insets in (b)–(d) show SAED patterns while lower insets in (c) and (d) are high-resolution HAADF-STEM and TEM images, respectively. The white arrows in (c) show grain boundaries between c- and t-GSTO as well as the indicate (0001) planes of t-GSTO.

samples without LSMO content (Fig. S3 in Supporting Information). Thus, surplus of oxygen in alloyed thin films tend to form various oxides with Mn, La or Sr with subsequent phase separation (see more discussion below), rather than to incorporate into the GSTO crystallites. A line scan revealed that the concentrations of oxygen and tellurium over a wide range are in reciprocal ratio to each other. This may either indicate that some tellurium is exchanged with oxygen and occupies the anion sites in the GST structure, or it could indicate a phase separation into an oxygen-rich phase and a phase depleted of oxygen. It was reported that oxygen cannot be exchanged very well because of the comparatively small ion radius but would instead occupy the tetrahedral sites. Since these sites in the cubic structure are too small, this causes distortions, which change the optical properties of the thin films. It must be noted though that the occupation of the tetrahedral sites has only been concluded from the optical properties and has never been directly measured and there is no structure solution of GST containing oxygen. A phase separation is the still the more probable explanation.

The microstructure of GSTO-LSMO(14 W) and GSTO-LSMO(21 W) thin films look significantly different compared to the above-mentioned samples. No large crystals are visible in bright-field TEM images (e.g. Fig. 3d) and the both samples possess similar microstructure. However, the largest identified crystals in GSTO-LSMO(14 W) and GSTO-LSMO(21 W) samples are 20 nm and 10 nm, respectively. The crystallites are embedded in an amorphous oxide matrix (see inset into Fig. 3d). SAED pattern of Fig. 3d displays diffraction rings instead of isolated reflections as in Fig. 3b. All diffraction spots belong to the cubic GST phase. No large trigonal crystals were observed. Consequently, higher concentration of La, Sr, Mn and O impact the phase formation of GST alloy and improve thermal stability of the alloy. Overall, TEM measurements are in a good agreement with the average structure of the studied thin films obtained by XRD studies (Fig. S4 in Supporting Information). The XRD showed that the highly alloyed with LSMO thin films (14 W and 21 W) possess the cubic crystal structure of GST even when crystallized at temperatures higher than 250 °C. At 350 °C the samples with low LSMO content (0 W, 8 W) revealed the diffraction spots of the trigonal modification of GST structure, while the other two samples still indicated only broad diffraction spots of the cubic modification, pointing out nanocrystalline nature of the GSTO grains. No other crystalline phases were identified by XRD.

3.3. Chemical bonding

Further studies concentrate on XPS measurements, which are applied to identify the chemical bonding relations between the elements of GSTO-LSMO composite thin films. Generally, every element shows different binding energies depending on the energy level (orbital

occupied by electrons. Since some of these energy levels may overlap, it was necessary to use the peaks of the spectrum that could be clearly assigned to one element.

Strontium, lanthanum, manganese, antimony and tellurium show the same binding energies in the amorphous and crystallized samples. Tellurium reveals its $3d_{5/2}$ peak at 572.6 eV (Fig. 4a), which indicates that it is metallically bonded to other tellurium atoms. Antimony shows its $3d_{5/2}$ peak at 528.5 eV (Fig. 4b). This can be assigned to Sb–Ge bonds. There is also a peak at a slightly higher binding energy, which would be equal to the antimony oxide (Sb_2O_3) peak at 530.5 eV [47], but this peak is caused by the oxygen 1 s energy level. The peak grows with increasing co-sputtering power because on the one hand the oxygen amount is increased, and on the other hand, antimony forms Sb–O bonds. From the different height of the peak in the highly alloyed samples it is concluded that in the amorphous samples there are more Sb–O bonds present, because the oxygen content is similar as EDX exposed (Fig. 1).

The $Sr3d_{5/2}$ peak is at 133.7 eV (Fig. 4c) and fits neither to Sr–O bonds nor Sr–Sr bonds. Sr–Sr bonds and Sr–O would lead to higher binding energies of 134.3 eV and 135.3 eV, respectively. In this case, there should be chemical bonds apparent to elements with higher electronegativity than Sr, because of the raised binding energy. Elements with a considerably higher electronegativity would be germanium, antimony and tellurium. If strontium was incorporated into the crystal structure of GST it should occupy, as an element with such low electronegativity and fitting ion radius, the cation positions. This would imply bonding to germanium and antimony. Sr–Te bonds can also be excluded because there is no indication at the $Te3d_{5/2}$ peak for another element being bonded to tellurium.

The manganese $2p_{3/2}$ and $2p_{1/2}$ peaks lay at 641.2 eV and 653 eV, respectively (Fig. 4d) and does not change with LSMO content or during crystallization. This indicates manganese having oxygen bonds for all sputtering rates and forms the MnO [48]. The lanthanum $3d_{5/2}$ peak is located at 834.9 eV (Fig. 4e). Lanthanum shows a multiplet splitting at the 3d energy levels, caused by electrons from inner orbitals (in this case $O2p$) occupying the normally vacant 4f orbitals in the lanthanum atoms (Fig. 4e). This results in an additional, slightly higher, energy level. The binding energies at 834.9 eV and 851.7 eV, however, show the La–O bonds and the La_2O_3 compound correspondingly [49]. Thus, lanthanum is only bonded to oxygen in every sample.

The XPS spectrum of Ge with its $2p_{3/2}$ peak is shown in Fig. 4f. For the pure GSTO and low alloyed GSTO-LSMO(4 W) samples, the germanium $2p_{3/2}$ peak is at 1217.9 eV. The peak fits the reported value for metallic Ge [50]. However, the peak themselves reveals a shoulder towards higher binding energy, suggesting the presence of Ge–O bonds. The highest alloyed GSTO-LSMO (21 W) thin films show binding energies at 1219.7 and 1219.0 eV for amorphous and crystalline phases,

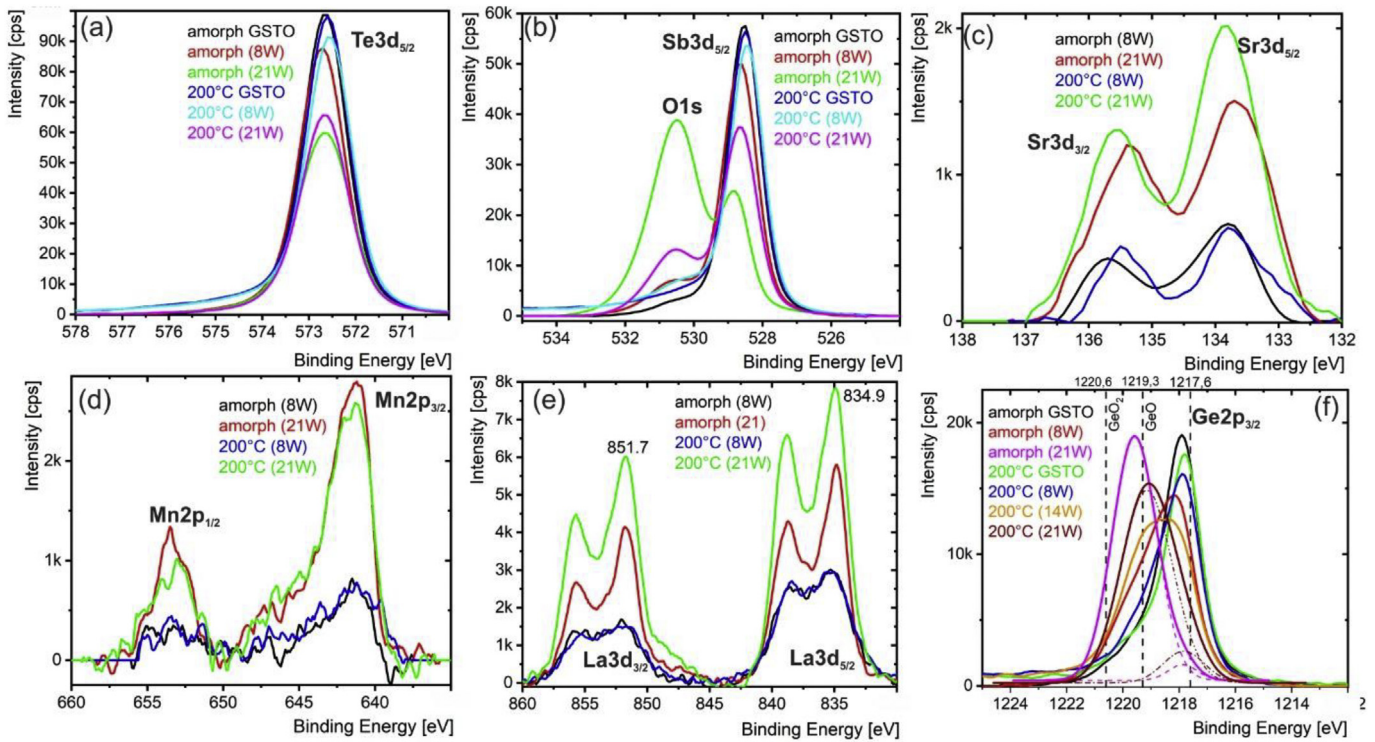


Fig. 4. XPS spectra for (a) $\text{Te}3d_{5/2}$, (b) $\text{Sb}3d_{5/2}$ together with O1s peak, (c) Sr3d peaks, (d) Mn2p peaks, (e) La3 peaks and (f) $\text{Ge}2p_{3/2}$ peak.

respectively. However, the peaks itself are not Gaussian and consists of two components. This is a sign for more than one bonding partner. A peak fitting procedure for both peaks shows the major components of each peak at 1219.6 eV and 1219.4 eV, respectively, and the second component at 1217.8 eV. Thus, the first component fits better to the GeO while the second component belongs to metallic Ge [50]. Less alloyed GSTO-LSMO (14 W) sample exhibits similar two components at 1218.9 eV and 1217.8 eV as the highest alloyed sample.

Overall, the results of the XPS measurements confirm the outcomes of EDX data and reveals the formation of various oxides. Thus, it can be concluded that a phase separation is happening into an oxide enriched and an oxide depleted phase. The oxide rich phase is formed by oxides such as GeO, La_2O_3 , Sb_2O_3 and MnO. In addition, XPS results indicate incorporation of Sr into GSTO crystal structure.

3.4. Electrical measurements and resistive switching behavior

Fig. 5a shows temperature-dependent sheet resistance measurements of pure and LSMO alloyed GSTO thin films. The sheet resistance values (Ω) for amorphous thin films at room temperature are $5.1 \times 10^7 \Omega$ for pure GSTO sample, $3.2 \times 10^8 \Omega$ for medium alloyed GSTO-LSMO(8 W) thin film and $6 \times 10^9 \Omega$ for highest alloyed GSTO-LSMO(21 W) sample. This shows two orders of magnitude higher initial resistance for the highest alloyed sample and is associated with higher concentration of high- κ dielectric La_2O_3 oxide in the composite thin films. Moreover, the sheet resistance of crystalline state of the highest alloyed thin film is also approximately two orders of magnitude higher than that of the unalloyed sample. Such high values of sheet resistance is beneficial for memory devices since the Joule heating effect in high resistive materials increases, which leads to the reduction of the programming currents of working PCM based devices [4,13].

The sheet resistance continuously decreases with increasing of heating temperature and suddenly drops at a temperature of $\sim 168^\circ\text{C}$ for pure GSTO thin film, at a temperature of 190°C for medium alloyed GSTO-LSMO(8 W) sample as well as a temperature of 200°C for highest

alloyed GSTO-LSMO(21 W) sample. This shows phase transition from amorphous to crystalline cubic phase. The transition is completed at heating temperatures of 177°C for pure GSTO thin film, 205°C for medium alloyed GSTO-LSMO(8 W) sample and 225°C for the most highly alloyed GSTO-LSMO(21 W) sample. Such high transition temperature for the most highly alloyed thin film shows the most highly thermal stability of the composite, which is beneficial for embedded applications and for devices with reduced power consumption. Pure GSTO, low alloyed GSTO-LSMO(4 W) and medium alloyed GSTO-LSMO(8 W) thin films revealed second drop of the sheet resistance at heating temperatures of 288°C , 370°C and 398°C , respectively. These temperatures are associated with structural transition from the metastable cubic phase to the stable trigonal phase, which is in line with TEM observations. Contrary, GSTO-LSMO(14 W) and GSTO-LSMO(21 W) thin films did not show the second phase transition up to a heating temperature of 400°C revealing the presence of the cubic phase in the samples only. The estimated transition temperature to the trigonal phase for the highest alloyed sample from Fig. 5(a) is 438°C .

For memory applications, it is necessary to study switching characteristics of prepared nanocomposite thin films. Since GSTO-LSMO (21 W) thin film shows the most highest thermal stability besides the studied compositions, the thin film was selected to investigate their resistive switching behavior. For this purpose, electrochemical metallization (ECM) cell utilizing Ag thin layer as the bottom electrode and W tip with diameter of $15 \mu\text{m}$ as the top electrode was prepared. Fig. 5 (b) shows I-V curves for the GSTO-LSMO(21 W) based ECM device. The cell reveals bipolar resistive switching without an initial electroforming step. While the positive voltage induces SET transition with gradual decrease in the resistance, the negative voltage causes RESET transition and the increase of resistance. By varying the applied bias voltage from $\pm 0.2 \text{ V}$ to $\pm 1 \text{ V}$ different resistance states can be accessed. The endurance performance of the ECM cell is shown in the Fig. 5(d). The LRS/HRS ratio of the device was approximately one order of magnitude retained over 120 cycles, which is good for data storage applications. It is likely that the resistance window can be

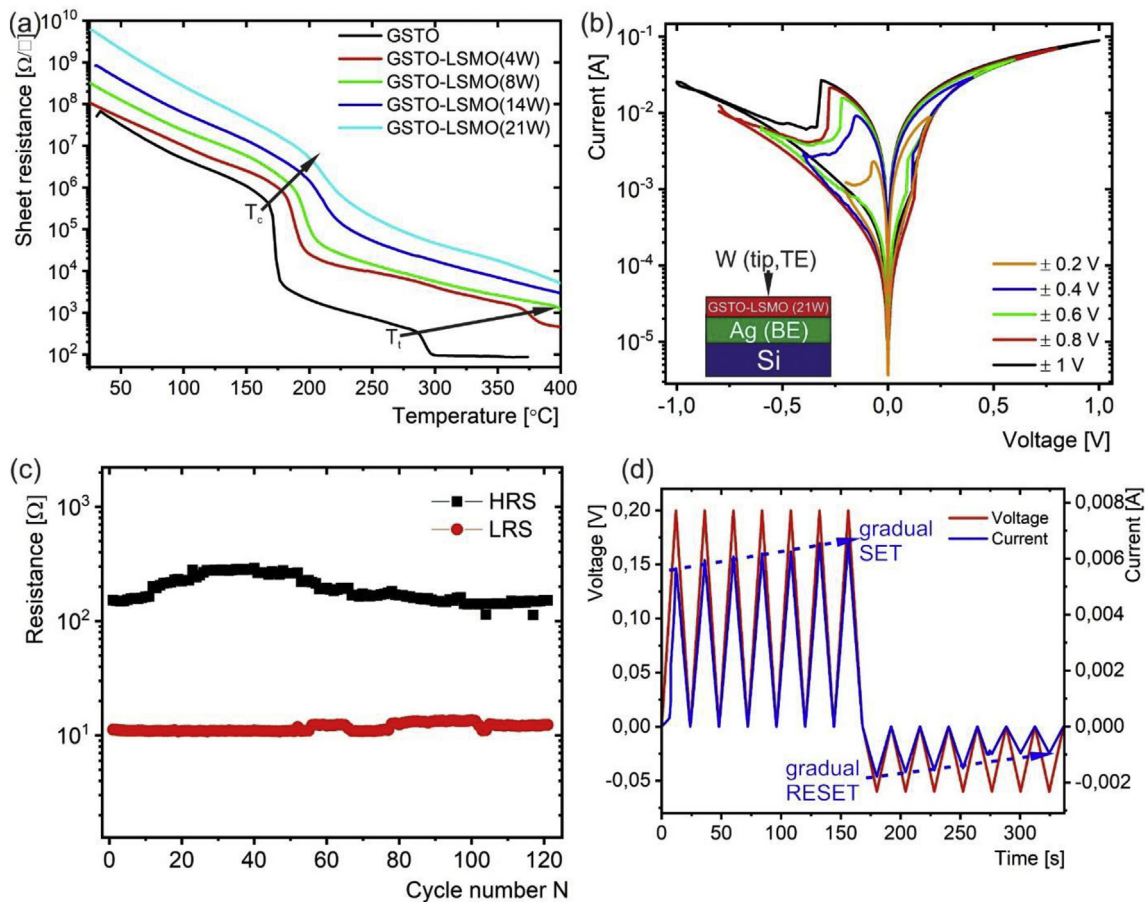


Fig. 5. (a) Sheet resistance measurements of GSTO and GSTO-LSMO composite thin films. The sheet resistance decreases significantly upon the transition from the amorphous to the crystalline phase. Addition of LSMO results in a pronounced increase of transition temperature. (b) I-V curves for GSTO-LSMO(21 W) based ECM cell under bipolar resistive switching using different voltages. The cell is shown in the inset. (c) Endurance measurements of the ECM device with ± 1 V DC cycles and read voltage of 0.1 V. (d) I-t and V-t curves showing the gradual increase and decrease of current with time.

increased using smaller electrodes [51,52]. Moreover, to study the synaptic behavior of the GSTO-LSMO(21 W) based ECM device, consecutive voltage cycles were applied to the cell first in positive and then in negative voltage directions. By applying a constant voltage, an increase in current is measured after each cycle (Fig. 5(d)). By repeated voltage cycling from 0 to 0.2 V, an increase in current is measured after each cycle. By following cycling from 0 to -0.06 V, the responding current decreases gradually. This cell response can be used to mimic synaptic behaviors of biological systems, i.e. potentiation and depression. Consequently, GSTO-LSMO

(21 W) material has potential for applications in neuromorphic computing [53]. The switching mechanisms in such ECM cell were attributed to the electrochemical formation of conductive percolation network developed by dissolved Ag ions from the electrode material [54].

3.5. Optical measurements

Pure GSTO and alloyed GSTO-LSMO were also studied by UV-Vis spectroscopy to obtain absorption spectra. The resulting spectra are

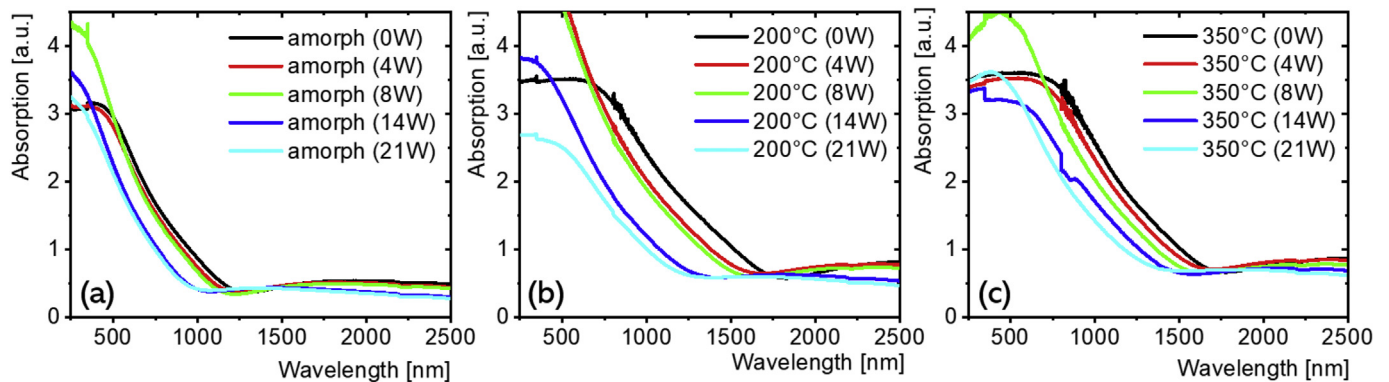


Fig. 6. Absorption spectra for amorphous and crystallized at different temperatures GSTO-LSMO thin films; (a) Amorphous samples, (b) thin films crystallized at a temperature of 200 $^{\circ}\text{C}$ and (c) samples crystallized at a temperature of 350 $^{\circ}\text{C}$. Values above 5 are beyond the detection limit; so absorptions above 99.999% could not be detected and the values in this range are therefore neglectable.

shown in Figs. 6a–b in the range between 250 nm and 2500 nm. The curves are shifted to lower wavelengths and show a decrease in the absorption with increasing the content of LSMO. The transparency also depends on the crystallization temperature and crystal phase. Depending on the crystal structure, the GSTO-LSMO thin films exhibit different absorption behavior in the Vis and NIR regions. The amorphous samples are more transparent in these regions than the crystalline samples. There are differences in the absorption spectra between the crystalline samples. So, the GSTO-LSMO composite thin films crystallized at a temperature of 200 °C are more transparent than the composite thin films crystallized at a temperature of 350 °C. The transmission values for amorphous and crystalline thin films (crystallized at 200 °C) at a wavelength of 1550 nm are shown in Fig. S5 of Supporting Information. Although the differences in transmission between amorphous and crystalline states decrease with increasing of LSMO content, the differences are still large enough to distinguish between the different states. The optical band gaps calculated from the Fig. 6 are shown in Table 1. The band gaps depend on the sample states and crystallization temperature. The optical band gaps of the GSTO-LSMO composites widen as the proportion of LSMO in the composite thin films increases, showing a possibility of band gap engineering of the phase change alloys. In addition, crystalline thin films possess lower values of band gaps than the amorphous thin films. Overall, the optical measurements reveal that the Vis-NIR transmission spectra of the GSTO-LSMO composite thin films depends on the amount of LSMO and crystal phase. This shows the suitability of such LSMO-GSTO composites for applications in tunable photonics in the Vis-NIR spectral ranges.

4. Conclusions

This work reports on the preparation and study of the microstructure, local structure, electrical and optical properties of pure Ge-Sb-Te-O (GSTO) and alloyed with La-Sr-Mn-O (LSMO) thin films. The outcomes reveal that LSMO content impact crystal size and crystallization behavior of GSTO-LSMO composites. Thermal heating of amorphous samples at a temperature of 200 °C resulted in the crystallization of metastable GSTO phase with crystal sizes in the range of 20 nm for unalloyed thin films and of 5–10 nm for alloyed nanocomposites. While the formation of large voids caused by thermal migration during thermal-induced crystallization process and large grains are observed in pure GSTO sample after thermal heating at a temperature of 350 °C, the GSTO-LSMO composite thin films showed no void formation and revealed the suppression in the formation of high-temperature stable trigonal GSTO phase in highly alloyed samples. Analysis of local chemical bonding by X-ray spectroscopy reveal the presence of different oxides (GeO, La₂O₃, Sb₂O₃ and MnO) in the alloyed thin films, while Sr atoms are found to be incorporated into the GSTO crystallites. Moreover, the alloying of GSTO with LSMO oxide enhances the thermal stability of the amorphous phase and increases the resistances of amorphous and crystalline phase of GSTO-LSMO composite thin films. ECM memory device made of GSTO-LSMO thin film shows bipolar switching and synaptic behavior. Vis-NIR absorption spectra of the GSTO-LSMO thin films move to lower wavelengths and band gap widens with increasing the LSMO content. Overall, the results of this work reveal the highly promising potential of GSTO-LSMO nanocomposites for data storage and reconfigurable photonic applications as well as neuromorphic computing.

Declaration of Competing Interest

The authors declare that they have no known competing financial interests or personal relationships that could have appeared to influence the work reported in this paper.

Acknowledgments

The authors would like to thank Mrs. A. Mill for her assistance in the preparation of specimens for TEM investigations. This work was financially supported by the National Natural Science Foundation of China (Grant No. 62074089), Natural Science Foundation of Zhejiang Province, China (Grant No. LY20F040002), the Natural Science Foundation of Ningbo City, China (Grant No. 2019A610059), the Fundamental Research Funds for the Provincial Universities of Zhejiang (Grant No. SJLY2021013) and was sponsored by the K. C. Wong Magna Fund in Ningbo University.

Appendix A. Supplementary data

Supplementary data to this article can be found online at <https://doi.org/10.1016/j.matdes.2020.109392>.

References

- [1] M. Wuttig, N. Yamada, Phase-change materials for rewriteable data storage, *Nat. Mater.* 6 (2007) 824–832.
- [2] S. Raoux, W. Welnic, D. Ielmini, Phase change materials and their application to non-volatile memories, *Chem. Rev.* 110 (2010) 240–267.
- [3] S. Raoux, F. Xiong, M. Wuttig, E. Pop, Phase change materials and phase change memory, *MRS Bull.* 39 (2014) 703–710.
- [4] P. Noé, C. Vallée, F. Hippert, F. Fillot, J.-Y. Raty, Phase-change materials for non-volatile memory devices: from technological challenges to materials science issues, *Semicond. Sci. Technol.* 33 (2018), 013002, .
- [5] A. Lotnyk, M. Behrens, B. Rauschenbach, Phase change thin films for non-volatile memory applications, *Nanoscale Advances*. 1 (2019) 3836–3857.
- [6] F. Yeung, S.-J. Ahn, Y.-N. Hwang, C.-W. Jeong, Y.-J. Song, S.-Y. Lee, et al., Ge₂Sb₂Te₅ Confined structures and integration of 64 Mb phase-change random access memory, *Jpn. J. Appl. Phys.* 44 (2005) 2691–2695.
- [7] A. Babich, A. Sherchenkov, S. Kozyukhin, P. Lazarenko, O. Boytsova, A. Shuliatyev, Effect of doping on the crystallization kinetics of phase change memory materials on the basis of Ge–Sb–Te system, *J. Therm. Anal. Calorim.* 127 (2017) 283–290.
- [8] Y. Gu, S. Song, Z. Song, Y. Cheng, X. Du, B. Liu, et al., SixSb₂Te materials with stable phase for phase change random access memory applications, *J. Appl. Phys.* 111 (2012) 054319–8.
- [9] S. Privitera, E. Rimini, R. Zonca, Amorphous-to-crystal transition of nitrogen- and oxygen-doped Ge₂Sb₂Te₅ films studied by in situ resistance measurements, *Appl. Phys. Lett.* 85 (2004) 3044–3046.
- [10] X. Li, H. Chen, C. Xie, D. Cai, S. Song, Y. Chen, et al., Enhancing the performance of phase change memory for embedded applications, *Phys Status Solidi RRL*. 13 (2019) 1800558.
- [11] N. Matsuzaki, K. Kurotsuchi, Y. Matsui, O. Tonomura, N. Yamamoto, Y. Fujisaki, et al., Oxygen-doped GeSbTe phase-change memory cells featuring 1.5 V/100–/spl mu/m/A standard 0.13/spl mu/m CMOS operations, *IEEE International Electron Devices Meeting*, 2005 IEDM Technical Digest 2005, pp. 738–741.
- [12] Hubert Q. Jahan C, Toffoli A, Navarro G, Chandrashekar S, Noe P, et al. Lowering the Reset Current and Power Consumption of Phase-Change Memories with Carbon-Doped Ge₂Sb₂Te₅. 2012 4th IEEE International Memory Workshop 2012. p. 1–4.
- [13] Horii H, Yi JH, Park JH, Ha YH, Baek IG, Park SO, et al. A novel cell technology using N-doped GeSbTe films for phase change RAM. 2003 Symposium on VLSI Technology Digest of Technical Papers (IEEE Cat No03CH37407) 2003. p. 177–8.
- [14] D.Z. Dimitrov, Y.-H. Lu, M.-R. Tseng, W.-C. Hsu, H.-P.D. Shieh, Oxygen and nitrogen co-doped GeSbTe thin films for phase-change optical recording, *Jpn. J. Appl. Phys.* 41 (2002) 1656–1659.
- [15] M.H. Jang, S.J. Park, D.H. Lim, M.-H. Cho, K.H. Do, D.-H. Ko, et al., Phase change behavior in oxygen-incorporated Ge₂Sb₂Te₅ films, *Appl. Phys. Lett.* 95 (2009), 012102, .
- [16] X. Zhou, W. Dong, H. Zhang, R.E. Simpson, A zero density change phase change memory material: GeTe-O structural characteristics upon crystallisation, *Sci. Rep.* 5 (2015) 11150.
- [17] X. Zhou, Y. Du, J.K. Behera, L. Wu, Z. Song, R.E. Simpson, Oxygen tuned local structure and phase-change performance of germanium telluride, *ACS Appl. Mater. Interfaces* 8 (2016) 20185–20191.
- [18] C. Rivera-Rodríguez, E. Prokhorov, G. Trapaga, E. Morales-Sánchez, M. Hernandez-Landaverde, Y. Kovalenko, et al., Mechanism of crystallization of oxygen-doped amorphous Ge₁Sb₂Te₄ thin films, *Journal of Applied Physics* 96 (2004) 1040–1046.
- [19] J. González-Hernández, P. Herrera-Fierro, B. Chao, Y. Kovalenko, E. Morales-Sánchez, E. Prokhorov, Structure of oxygen-doped Ge:Sb:Te films, *Thin Solid Films* 503 (2006) 13–17.
- [20] G. Wang, Y. Zhang, C. Li, A. Lotnyk, Y. Lu, X. Shen, Self-limited growth of Nanocrystals in structural heterogeneous phase-change materials during the heating process, *Cryst. Growth Des.* 19 (2019) 1356–1363.
- [21] G. Wang, H. Wang, A. Lotnyk, R. Wang, X. Shen, Unique interface-driven crystallization mechanism and element-resolved structure imaging of ZnO-Ge₂Sb₂Te₅ nanocomposites, *Ceram. Int.* 44 (2018) 22497–22503.
- [22] D. Dimitrov, H.P.D. Shieh, The influence of oxygen and nitrogen doping on GeSbTe phase-change optical recording media properties, *Mater. Sci. Eng. B* 107 (2004) 107–112.

- [23] M. Tai, M. Kinoshita, T. Ohyanagi, T. Morikawa, K. Akita, N. Takaura, Fabrication process for pillar GeTe/Sb₂Te₃superlattice topological-switching random access memory, *Japanese Journal of Applied Physics* 54 (2015) 05ED1.
- [24] R.E. Simpson, P. Fons, A.V. Kolobov, T. Fukaya, M. Krbal, T. Yagi, et al., Interfacial phase-change memory, *Nat. Nanotechnol.* 6 (2011) 501–505.
- [25] J. Feng, A. Lotnyk, H. Bryja, X. Wang, M. Xu, Q. Lin, et al., "stickier"-surface Sb₂Te₃ templates enable fast memory switching of phase change material GeSb₂Te₄ with growth-dominated crystallization, *ACS Appl. Mater. Interfaces* 12 (2020) 33397–33407.
- [26] F. Jiao, B. Chen, K. Ding, K. Li, L. Wang, X. Zeng, et al., Monatomic 2D phase-change memory for precise neuromorphic computing, *Appl. Mater. Today* 20 (2020) 100641.
- [27] Wang WJ, Loke D, Law LT, Shi LP, Zhao R, Li MH, et al. Engineering grains of Ge₂Sb₂Te₅ for realizing fast-speed, low-power, and low-drift phase-change memories with further multilevel capabilities. 2012 International Electron Devices Meeting2012. p. 31.3.1–.3.4.
- [28] D. Loke, T.H. Lee, W.J. Wang, L.P. Shi, R. Zhao, Y.C. Yeo, et al., Breaking the speed limits of phase-change memory, *Science*. 336 (2012) 1566–1569.
- [29] M. Behrens, A. Lotnyk, J.W. Gerlach, M. Ehrhardt, P. Lorenz, B. Rauschenbach, Direct measurement of crystal growth velocity in epitaxial phase-change material thin films, *ACS Appl. Mater. Interfaces* 11 (2019) 41544–41550.
- [30] T.-Y. Lee, K.H.P. Kim, D.-S. Suh, C. Kim, Y.-S. Kang, D.G. Cahill, et al., Low thermal conductivity in Ge₂Sb₂Te₅-SiO_x for phase change memory devices, *Appl. Phys. Lett.* 94 (2009) 243103.
- [31] D. Lee, S.-S. Yim, H.-K. Lyeo, M.-H. Kwon, D. Kang, H.-G. Jun, et al., Formation of Ge₂Sb₂Te₅-TiO_x Nanostructures for Phase Change Random Access Memory Applications, *Electrochemical and Solid State Letters* 13 (2010) K8.
- [32] S. Song, Z. Song, L. Wu, B. Liu, S. Feng, Stress reduction and performance improvement of phase change memory cell by using Ge₂Sb₂Te₅-TaO_x composite films, *J. Appl. Phys.* 109 (2011), 034503, .
- [33] J.P. Reifenberg, D.L. Kencke, K.S. Goodson, The impact of thermal boundary resistance in phase-change memory devices, *IEEE Electron Device Letters*. 29 (2008) 1112–1114.
- [34] T.-Y. Lee, S.-S. Yim, D. Lee, M.-H. Lee, D.-H. Ahn, K.-B. Kim, Separate domain formation in Ge₂Sb₂Te₅-SiO_x mixed layer, *Appl. Phys. Lett.* 89 (2006) 163503.
- [35] S.W. Ryu, J.H. Oh, B.J. Choi, S.-Y. Hwang, S.K. Hong, C.S. Hwang, et al., SiO₂ incorporation effects in Ge₂Sb₂Te₅ films prepared by magnetron sputtering for phase change random access memory devices, *Electrochem. Solid-State Lett.* 9 (2006) G259.
- [36] S. Song, Z. Song, B. Liu, L. Wu, S. Feng, Performance improvement of phase-change memory cell with Ge₂Sb₂Te₅-HfO₂ composite films, *Applied Physics A*. 99 (2010) 767–770.
- [37] S. Song, Z. Song, B. Liu, L. Wu, S. Feng, Ge₂Sb₂Te₅ and PbZr_{0.30}Ti_{0.70}O₃ composite films for application in phase change random access memory, *Mater. Lett.* 64 (2010) 317–319.
- [38] R. Shayduk, H. Navirian, W. Leitenberger, J. Goldshteyn, I. Vrejoiu, M. Weinelt, et al., Nanoscale heat transport studied by high-resolution time-resolved x-ray diffraction, *New J. Phys.* 13 (2011), 093032, .
- [39] H.-K. Lyeo, D.G. Cahill, B.-S. Lee, J.R. Abelson, M.-H. Kwon, K.-B. Kim, et al., Thermal conductivity of phase-change material Ge₂Sb₂Te₅, *Appl. Phys. Lett.* 89 (2006) 151904.
- [40] K.S. Siegert, F.R. Lange, E.R. Sittner, H. Volker, C. Schlockermann, T. Siegrist, et al., Impact of vacancy ordering on thermal transport in crystalline phase-change materials, *Rep. Prog. Phys.* 78 (2015), 013001, .
- [41] A. Urushibara, Y. Moritomo, T. Arima, A. Asamitsu, G. Kido, Y. Tokura, Insulator-metal transition and giant magnetoresistance in La_{1-x}Sr_xMnO₃, *Phys. Rev. B* 51 (1995) 14103–14109.
- [42] M.Z. Zarbali, A. Göka, I.H. Mutlu, S. Kazan, A.I. Sale, F.A. Mikailzade, Structure and Magnetic Properties of La_{0.66}Sr_{0.33}MnO₃ Thin Films Derived Using Sol-Gel Technique, *Journal of Superconductivity and Novel Magnetism* 25 (2012) 2767–2770.
- [43] S. Koohfar, A.B. Georgescu, A.N. Penn, J.M. LeBeau, E. Arenholz, D.P. Kumah, Confinement of magnetism in atomically thin La_{0.7}Sr_{0.3}CrO₃/La_{0.7}Sr_{0.3}MnO₃ heterostructures, *npj Quantum Materials* 4 (2019) 25.
- [44] U. Ross, A. Lotnyk, E. Thelander, B. Rauschenbach, Direct imaging of crystal structure and defects in metastable Ge₂Sb₂Te₅ by quantitative aberration-corrected scanning transmission electron microscopy, *Appl. Phys. Lett.* 104 (2014) 121904.
- [45] X. Sun, M. Ehrhardt, A. Lotnyk, P. Lorenz, E. Thelander, J.W. Gerlach, et al., Crystallization of Ge₂Sb₂Te₅ thin films by nano- and femtosecond single laser pulse irradiation, *Sci. Rep.* 6 (2016) 28246.
- [46] U.H. Roß, Structural Investigation of Ge-Sb-Te Thin Films by Aberration-Corrected Scanning Transmission Electron Microscopy: Kiel University (CAU), https://macau.uni-kiel.de/receive/diss_mods_00021329 2017.
- [47] K.-S. Hong, D.-H. Nam, S.-J. Lim, D. Sohn, T.-H. Kim, H. Kwon, Electrochemically synthesized Sb/Sb₂O₃ composites as high-capacity anode materials utilizing a reversible conversion reaction for Na-ion batteries, *ACS Appl. Mater. Interfaces* 7 (2015) 17264–17271.
- [48] E.S. Ilton, J.E. Post, P.J. Heaney, F.T. Ling, S.N. Kerisit, XPS determination of Mn oxidation states in Mn (hydr)oxides, *Appl. Surf. Sci.* 366 (2016) 475–485.
- [49] M.F. Sunding, K. Hadidi, S. Diplas, O.M. Løvvik, T.E. Norby, A.E. Gunnæs, XPS characterisation of in situ treated lanthanum oxide and hydroxide using tailored charge referencing and peak fitting procedures, *J. Electron Spectrosc. Relat. Phenom.* 184 (2011) 399–409.
- [50] K. Prabhakaran, T. Ogino, Oxidation of Ge(100) and Ge(111) surfaces: an UPS and XPS study, *Surf. Sci.* 325 (1995) 263–271.
- [51] S. Yoo, T. Eom, T. Gwon, C.S. Hwang, Bipolar resistive switching behavior of an amorphous Ge₂Sb₂Te₅ thin films with a Te layer, *Nanoscale*. 7 (2015) 6340–6347.
- [52] Z. Zhang, Y. Wang, G. Wang, J. Mu, M. Ma, Y. He, et al., Electrochemical metallization cell with solid phase tunable Ge₂Sb₂Te₅ electrolyte, *Sci. Rep.* 8 (2018) 12101.
- [53] W. Zhang, R. Mazzarello, M. Wuttig, E. Ma, Designing crystallization in phase-change materials for universal memory and neuro-inspired computing, *Nature Reviews Materials*. 4 (2019) 150–168.
- [54] H. Bryja, C. Grüner, J.W. Gerlach, M. Behrens, M. Ehrhardt, B. Rauschenbach, et al., Impact of interfaces on bipolar resistive switching behavior in amorphous Ge-Sb-Te thin films, *J. Phys. D: Appl. Phys.* 53 (2020) 184002.